Localized states at the Rashba spin-orbit domain wall in magnetized graphene: Interplay of Rashba and magnetic domain walls

M. Inglot [1], J. Barnaś [2,3], V. K. Dugaev [1], and A. Dyrdał [2]

[1] *Department of Physics and Medical Engineering, Rzeszów University of Technology, al. Powstańców Warszawy 6, 35-959 Rzeszów, Poland*

[2] *Department of Mesoscopic Physics, ISQI, Faculty of Physics, Adam Mickiewicz University in Poznań, ul. Uniwersytetu Poznańskiego 2, 61-614 Poznań, Poland*

[3] *Institute of Molecular Physics, Polish Academy of Sciences, ul. M. Smoluchowskiego 17, 60-179 Poznań, Poland*

(Received 26 July 2023; revised 28 February 2024; accepted 22 March 2024; published 23 April 2024)

It is well known that electronic states in graphene with a uniform Rashba spin-orbit interaction and uniform magnetization, e.g., due to exchange coupling to a magnetic substrate, display an energy gap around the Dirac K and K' points. When the magnetization of graphene is nonuniform and forms a magnetic domain wall, electronic states localized at the wall emerge in the energy gap. In this paper we show that similar localized electronic states appear in the gap when the graphene is uniformly magnetized, while a domain wall appears in the Rashba spin-orbit interaction (i.e., opposite signs of the Rashba parameter on both sides of the wall). These electronic states propagate along the wall and are localized exponentially at the Rashba domain wall. They form narrow and nearly parabolic (at small wave vectors) bands, with relatively large effective electron mass. However, contrary to the magnetic domain wall, these states do not close the energy gap. We also consider the situation when the magnetic domain wall coexists with the Rashba domain wall, and both walls are localized at the same position. Electronic states due to the interplay of both domain walls are determined analytically and it is shown that the electronic states localized at the walls close the gap when a magnetic domain wall (symmetric or asymmetric) exists, independently of the Rashba parameter behavior.

DOI: 10.1103/PhysRevB.109.134435

I. INTRODUCTION

Electronic properties of graphene can be substantially modified by externally induced magnetization and Rashba spin-orbit interaction (SOI) due to proximity effects. It is well known that the interplay of perpendicular magnetization and Rashba SOI opens a gap in the electronic spectrum of graphene [1,2], making it semiconducting and therefore useful for various applications in two-dimensional (2D) electronics, spintronics, and optoelectronics [3,4]. Both magnetization and Rashba SOI can be induced in graphene due to proximity effects by encapsulation between thin layers of appropriate magnetic and semiconducting materials [5–17]. Domain walls (as well as topological excitations such as skyrmions) in the magnetic layer of such a hybrid structure remarkably modify the electronic properties of graphene, and can lead to additional states in the electronic spectrum. These states may determine new functionalities of graphene-based devices. This, in turn, paves the way to new possibilities of graphene applications, which are based on electric control of the domain wall/skyrmion motion—similar to the racetrack memory devices [18].

It has been shown theoretically that a magnetic domain wall in the magnetic cover layer on graphene with uniform Rashba SOI leads to electronic states that are exponentially localized at the wall [2]. These states emerge in the gap of bulk electronic spectrum created by the interplay of perpendicular magnetization and Rashba SOI. Interestingly, the localized states are characterized by a certain chirality, which leads to persistent current along the domain wall. This current is related to the corresponding quantum anomalous Hall (QAH) phase, and very likely it may be used in dissipationless electronics, similarly to heterostructures based on topological insulators [19,20]. The considerations in Ref. [2] assumed a very sharp (of atomic size) domain wall.

Domain walls and topological excitations that affect the electronic structure of graphene are not limited to magnetic ones, and can be also of other origins. For example, a superconducting layer on top of graphene induces a superconducting-pairing field [21]. It was shown that the topological excitations (e.g., vortices) in the superconducting layer can lead to localized electronic states in graphene as well [22,23].

Another example appears when using boron-nitrite (BN) as a substrate, which induces an effective sublattice-symmetry-breaking field and leads to a gap in the Dirac spectrum of graphene, Correspondingly, the stacking defects in the BN substrate can be considered as a sublattice domain wall. In the presence of spin-orbit interaction this domain wall can generate the edge states at the domain wall. Recent theoretical works have also shown that the domain walls between AB- and BA-stacked bilayer graphene can support protected chiral edge states related to the quantum valley Hall insulator phase [24–26]. It is worth to note that other domain walls were also investigated, e.g., in bilayer graphene systems, where domain walls separate two energetically equivalent Bernal stackings in the presence of an external magnetic field [27,28]. It has been found that such a domain wall substantially affects the

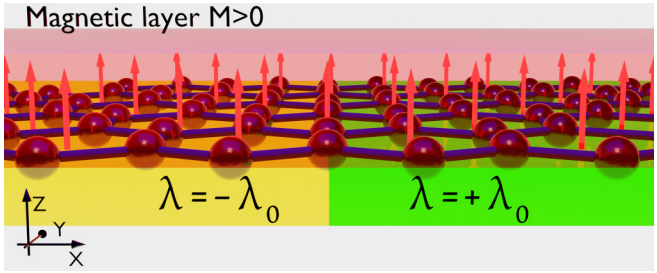

FIG. 1. Schematic picture of a uniformly magnetized graphene with a Rashba spin-orbit domain wall. The layer is in the x, y plane, with the axis y along the domain wall. In turn, the axis z is normal to the layer.

local electron density of states as well as electronic transport properties of graphene bilayers.

Recently, it has been shown [29] that the edge states associated with the domain walls of different origins in graphene are topologically protected, so that small variations of relevant parameters and/or scattering from impurities do not affect these states. It was found, e.g., that a domain wall associated with sign change in the valley-Zeeman spin-orbit coupling binds two robust Kramers pairs within the bulk gap due to the simultaneous presence of Rashba coupling.

An interesting situation is when the domain wall appears in the Rashba spin-orbit coupling, i.e., when the spin-orbit parameters on both sides of the wall have opposite signs. The effect of such a sharp spin-orbit domain wall on transport properties of electrons propagating across the domain wall was studied in Refs. [30,31]. Similar problem was also considered in Ref. [32], where, however, the domain wall was of mixed nature, i.e., on one side of the wall there was a nonzero magnetization and zero Rashba coupling, while on the other side the situation was reversed. Transport across such a wall revealed a significant anisotropic magnetoresistance.

In this paper we consider a van der Waals heterostructure consisting of a graphene monolayer deposited on a substrate that ensures strong Rashba spin-orbit interaction in the graphene. As the Rashba coupling can be easily tuned by external voltage, we assume that the substrate is gated with two electrodes, that create two domains with positive and negative Rashba coupling parameters, respectively. Such two domains with opposite Rashba parameters can be achieved with a structured substrate, as well. In addition, the Rashba coupling can be tuned by an external strain as well [33] and this also may be exploited in preparation of graphene with structured Rashba coupling. In turn, to create an exchange field in graphene, the structure is assumed to be covered by a magnetic layer with out-of-plane magnetization, e.g., by a monolayer of CrI_3 or another semiconducting 2D material with out-of-plane easy-axis magnetic anisotropy [6]. Schematically, the structure is presented in Fig. 1.

The edge states in the considered structure appear at the boundary between two different Rashba regions. Contrary to the case of magnetic domain wall, these states do not display chiral propagation and the corresponding dispersion relations are rather symmetric and similar to the parabolic ones. Moreover, these states do not close the gap, and for certain model parameters we find a very narrow (flat) band of edge states, which effectively describes heavy electrons (with large effective mass). It is known that the existence of such flat bands leads to many interesting physical phenomena such as superconductivity, ferromagnetism, etc. [34–42].

We also consider a more general situation, when the Rashba domain wall coexists with a magnetic domain wall localized at the same position. The effects due to interplay of both domain walls is studied in detail, and these effects are shown to depend on the strength of Rashba parameter and magnitude of magnetization on both sides of the walls.

The outline of the paper is as follows. In Sec. II we consider graphene with a model Rashba domain wall, and derive the electronic states localized exponentially at the wall. Properties of these states, including their spin polarization, are also analyzed there. The coexistence of Rashba and magnetic domain walls is studied in Sec. III. Transport along the wall is studied in Sec. IV, while summary and final conclusions are in Sec. V.

II. GRAPHENE WITH RASHBA DOMAIN WALL

In this section we consider graphene (atomic monolayer of carbon atoms) with Rashba SOI induced by a substrate. We assume two domains of the Rashba SOI, corresponding to opposite signs of the Rashba parameter λ, i.e., this parameter changes sign when crossing the boundary between the domains, referred to in the following as the Rashba domain wall. In addition we assume a magnetic overlayer with uniform magnetization normal to the graphene plane. The system is shown schematically in Fig. 1.

Hamiltonian for electrons in graphene near the valley K can be then written in the form

$$\hat{H} = -iv\left(\tau_x\nabla_x + \tau_y\nabla_y\right) + \lambda(x)\left(\tau_x\sigma_y - \tau_y\sigma_x\right) + \sigma_z M, \quad (1)$$

where τ_i and σ_i are the Pauli matrices acting in the sublattice and spin spaces, respectively, M is the magnetization-induced Zeeman-like field (for simplicity referred to in the following as magnetization) due to the proximity effect, with the magnetization along the z axis normal to the $x-y$ plane of graphene, while λ is the coupling constant of Rashba SOI, which changes sign at the interface $x = 0$ (see Fig. 1),

$$\lambda(x) = \begin{cases} -\lambda_0, & x < 0, \\ \lambda_0, & x > 0. \end{cases} \quad (2)$$

Finally, the parameter v in Eq. (1) is related to the electron velocity v_F in graphene, $v = \hbar v_F$ [43,44]. Without loss of generality we assume here $M > 0$ and $\lambda_0 > 0$. This assumption will be relaxed in Sec. III, when we will consider the coexistence of Rashba and magnetic domain walls.

A. Dispersion relation for the edge states

Now we look for solutions of the Schrödinger equation, $(\hat{H} - \varepsilon)\,\psi(\mathbf{r}) = 0$, which are localized at the domain wall. Since the parameter λ is uniform along the y axis and depends only on x, one can assume the wave function $\psi(x, y)$ in the form $\psi \sim e^{\kappa x}e^{ik_y y}$. The factor $e^{ik_y y}$ describes plane-wave propagation along the wall, while the factor $e^{\kappa x}$ describes

exponential localization of the wave function at the wall. To have the exponential localization on both sides, the parameter κ has to obey the following conditions: $\mathrm{Re}\,\kappa > 0$ for $x < 0$ and $\mathrm{Re}\,\kappa < 0$ for $x > 0$. Since the Schrödinger equation is in the matrix form, we look for its solution in the following bispinor form:

$$\psi^T(\mathbf{r}) = e^{ik_y y+\kappa x}(\varphi^\uparrow, \varphi^\downarrow, \chi^\uparrow, \chi^\downarrow) \tag{3}$$

separately in the regions $x < 0$ and $x > 0$. Upon substitution of Eq. (3) into the Schrödinger equation, one obtains the following four equations for the bispinor components:

$$\begin{aligned}
(M-\varepsilon)\,\varphi^\uparrow - iv\,(\kappa + k_y)\,\chi^\uparrow &= 0,\\
(M+\varepsilon)\,\varphi^\downarrow + 2i\lambda\chi^\uparrow + iv\,(\kappa + k_y)\,\chi^\downarrow &= 0,\\
iv\,(k_y-\kappa)\,\varphi^\uparrow - 2i\lambda\varphi^\downarrow + (M-\varepsilon)\,\chi^\uparrow &= 0,\\
iv\,(k_y-\kappa)\,\varphi^\downarrow - (M+\varepsilon)\,\chi^\downarrow &= 0,
\end{aligned} \tag{4}$$

where $\lambda = -\lambda_0$ for $x < 0$ and $\lambda = +\lambda_0$ for $x > 0$.

To have nonzero solutions, the determinant of the above set of linear equations must be equal to zero, which leads to the following equation for κ:

$$\begin{aligned}
&\kappa^4 v^4 - 2\kappa^2 v^2\left(v^2k_y^2 - M^2 - \varepsilon^2\right) + \left[(M-\varepsilon)^2 - v^2k_y^2\right]\\
&\quad\times\left[(M+\varepsilon)^2 - v^2k_y^2\right] + 4\lambda_0^2(M^2-\varepsilon^2) = 0.
\end{aligned} \tag{5}$$

Solutions of this equation take the form,

$$\begin{aligned}
\kappa_{1,2} &= \pm\frac{1}{v}\left(k_y^2v^2 - M^2 - \varepsilon^2 + 2\sqrt{\left(M^2+\lambda_0^2\right)\varepsilon^2 - M^2\lambda_0^2}\right)^{1/2},\\
\kappa_{3,4} &= \pm\frac{1}{v}\left(k_y^2v^2 - M^2 - \varepsilon^2 - 2\sqrt{\left(M^2+\lambda_0^2\right)\varepsilon^2 - M^2\lambda_0^2}\right)^{1/2}.
\end{aligned} \tag{6}$$

In the general case, κ can have real and imaginary parts. If the real parts are nonzero then $\mathrm{Re}\,\kappa_{1,3} > 0$ and $\mathrm{Re}\,\kappa_{2,4} < 0$. This means that in Eq. (3) we have to choose $\kappa = \kappa_1$ or κ_3 for $x < 0$ and $\kappa = \kappa_2$ or κ_4 for $x > 0$. With this choice, the wave function (3) decays as $|x| \to \infty$.

Solving Eqs. (4) for $x < 0$ and $x > 0$ with the corresponding λ and κ, we find the following possible solutions:

$$\psi_{1,3}(\mathbf{r}) = e^{\kappa_{1,3}x+ik_y y}\begin{pmatrix} 1\\ \dfrac{-k_y^2v^2 + v^2\kappa_{1,3}^2 + (M-\varepsilon)^2}{2v\lambda_0(k_y+\kappa_{1,3})}\\ -i\,\dfrac{M-\varepsilon}{v(k_y+\kappa_{1,3})}\\ i\,\dfrac{\left[-k_y^2v^2 + v^2\kappa_{1,3}^2 + (M-\varepsilon)^2\right](k_y-\kappa_{1,3})}{2\lambda_0(k_y+\kappa_{1,3})(\varepsilon+M)}\end{pmatrix} \tag{7}$$

for $x < 0$, and

$$\psi_{2,4}(\mathbf{r}) = e^{\kappa_{2,4}x+ik_y y}\begin{pmatrix} 1\\ -\dfrac{-k_y^2v^2 + v^2\kappa_{2,4}^2 + (M-\varepsilon)^2}{2v\lambda_0(k_y+\kappa_{2,4})}\\ -i\dfrac{M-\varepsilon}{v(k_y+\kappa_{2,4})}\\ -i\dfrac{\left[-k_y^2v^2 + v^2\kappa_{2,4}^2 + (M-\varepsilon)^2\right](k_y-\kappa_{2,4})}{2\lambda_0(k_y+\kappa_{2,4})(\varepsilon+M)}\end{pmatrix} \tag{8}$$

for $x > 0$. Using Eqs. (7) and (8), one can present the general solution corresponding to the edge state as the following superposition:

$$\psi(\mathbf{r}) = \begin{cases} A\psi_1 + B\psi_3, & x < 0,\\ C\psi_2 + D\psi_4, & x > 0,\end{cases} \tag{9}$$

where A, B, C, D are constants to be determined from the continuity of wave function at $x = 0$ (see also Appendix) and the normalization condition for $\psi(\mathbf{r})$.

The continuity condition at $x = 0$ leads to a system of four linear equations for the coefficients A, B, C, D, which has a nonzero solution when the corresponding determinant is zero. After rather cumbersome calculations we arrive at the following equation:

$$\frac{(-\varepsilon+M)\left[-\left\{\left(-2M^2-\lambda_0^2\right)\varepsilon^2 + M^2\lambda_0^2\right\}\xi(\zeta)\,\xi(-\zeta) + \lambda_0^2(-\varepsilon+M)(\varepsilon+M)\left(-v^2k_y^2 + M^2 + \varepsilon^2\right)\right]}{\lambda_0^2(\varepsilon+M)(M^2+\varepsilon^2-\zeta)(M^2+\varepsilon^2+\zeta)} = 0, \tag{10}$$

where $\xi(\zeta)$ is defined as $\xi(\zeta) = \sqrt{v^2k_y^2 - M^2 - \varepsilon^2 + \zeta}$ with $\zeta = 2\sqrt{(M^2+\lambda_0^2)\varepsilon^2 - M^2\lambda_0^2}$.

Equation (10) determines energy of the edge states as a function of k_y. There are two solutions of this equation, i.e.,

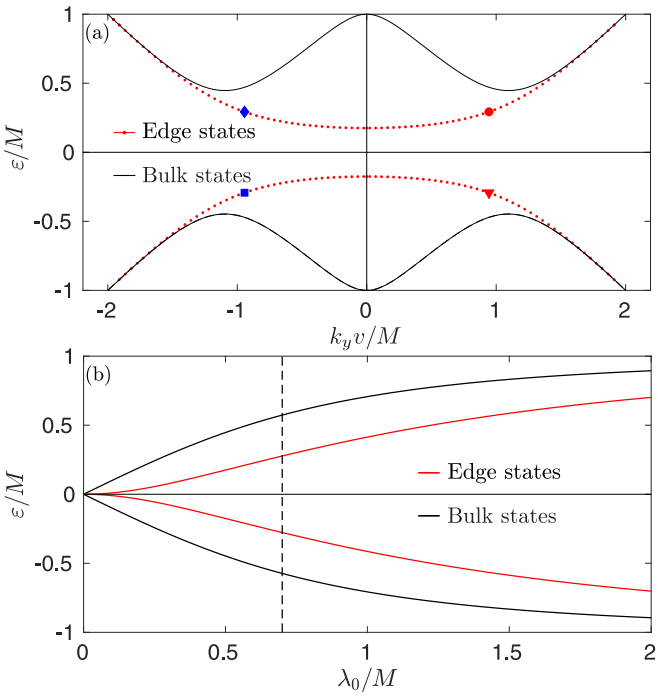

FIG. 2. (a) Dispersion curves of the edge states, $\varepsilon(k_y)$ (red dashed lines), for $\lambda_0 = 5$ meV and $M = 10$ meV, and (b) the dependence of $\varepsilon(k_y = 0)$ on the parameter λ_0. The solid black lines correspond to bulk bands. The dots in (a) indicate the points for which the spin polarization has been calculated, as will be discussed later. The vertical dashed line in (b) indicates the magnitude of λ_0/M used in the following when calculating the spin polarization.

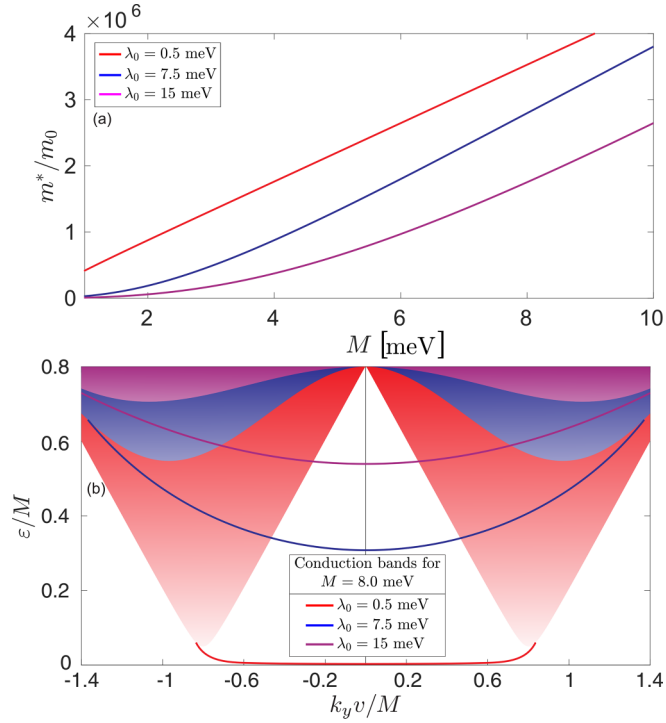

FIG. 3. (a) The effective electron mass in the edge states, m^*/m_0, corresponding to small values of k_y and presented as a function of magnetization M for indicated values of Rashba parameter. (b) Bulk bands (colored areas) and the corresponding edge states (lines of the same color as the corresponding bulk bands) for different values of λ_0, as indicated in the legend. For simplicity, only the bulk and edge states of positive energy are shown here.

$\pm\varepsilon(k_y)$. These solutions present the bands of edge states, shown in Fig. 2(a) by the red dotted lines. As one can see, there is an energy gap between the two bands of the edge states. In turn, Fig. 2(b) shows how the energy of edge states for zero wave vector, $\varepsilon(k_y = 0)$, grows with the parameter λ_0. This figure also reveals the fact that the gap between bulk (and also between the edge) states goes to zero for vanishing λ_0. Accordingly, the localized states disappear in the limit of $\lambda_0 \to 0$ because there is then no gap between the valence and conduction bands, and therefore the real parts of the parameters κ_i tend to zero.

To find the effective Hamiltonian for the edge states in the vicinity of $k_y = 0$ we use the $k - p$ method. For this purpose we define two basis functions

$$\psi^{(1)}(\mathbf{r}) = e^{ik_y y}\,\psi_0^{(1)}(x), \quad \psi^{(2)}(\mathbf{r}) = e^{ik_y y}\,\psi_0^{(2)}(x), \tag{11}$$

where $\psi_0^{(1,2)}(x)$ are the functions (9) with $k_y = 0$, corresponding to the eigenenergies $\varepsilon_{1,2} = \pm\varepsilon(0)$. Hence, we get for $i = 1, 2$,

$$\int_{-\infty}^{\infty} dx\, \psi_0^{(i)\dagger}(x)\, \hat{H}\, \psi_0^{(i)}(x) = \varepsilon_i(0) \tag{12}$$

as $\psi_0^{(1,2)}(x)$ are the eigenfunctions of Hamiltonian (1) corresponding to $k_y = 0$. Now, we calculate the matrix element

$$W_{12} = \int_{-\infty}^{\infty} dx\, \psi^{(1)\dagger}(\mathbf{r})\, \hat{H}\, \psi^{(2)}(\mathbf{r}), \tag{13}$$

which is not zero for $k_y \neq 0$ since the functions (11) are not eigenfunctions of the Hamiltonian (1) for $k_y \neq 0$.

Using the notation $W_{12} = k_y w$, one can write the equation for the edge states in the form of 1D Dirac equation with the effective Hamiltonian

$$H_{\text{eff}} = \begin{pmatrix} \Delta & k_y w \\ k_y w^* & -\Delta \end{pmatrix}, \tag{14}$$

where we denoted $\Delta = \varepsilon(0)$. For small values of k_y, the parameter w is constant, and can be calculated numerically. The energy spectrum of the above effective Hamiltonian is $\varepsilon(k_y) = \pm(\Delta^2 + k_y^2|w|^2)^{1/2}$, and the corresponding electron effective mass in the edge states is $m^* = \hbar^2\Delta/|w|^2$. The dependence of effective mass m^* on the Rashba parameter and magnetization M is presented in Fig. 3(a). This figure shows that the effective mass increases with increasing M and also with decreasing λ_0. The electron effective mass can be extremely large for small values of λ_0, which effectively corresponds to heavy electrons in a very narrow band. The corresponding dispersion curve of the edge states is then very flat, see the dispersion curve in Fig. 3(b) for $\lambda_0 = 0.5$ meV.

B. Spin polarization of the edge states

Having the wave function (9), one can calculate the corresponding probability density $|\psi_{k_y}(x)|^2$ of finding an electron

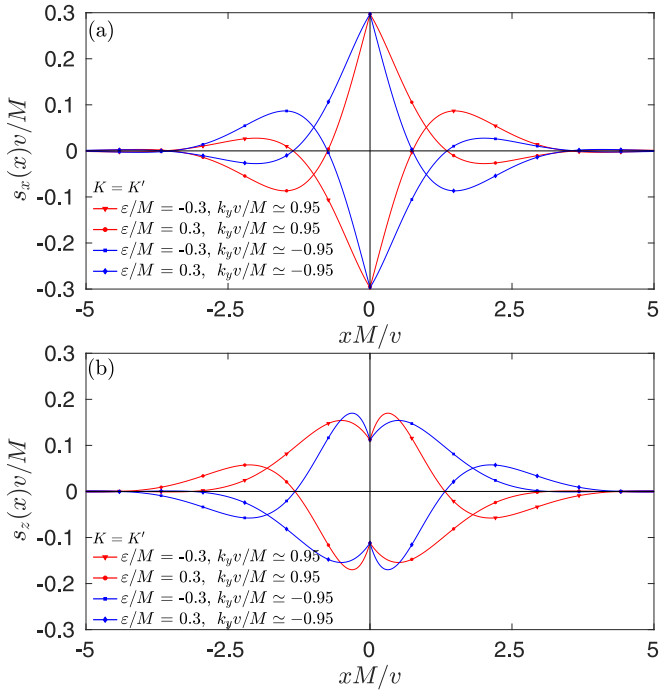

FIG. 4. Spin-density components (a) s_x and (b) s_z corresponding to the edge states for indicated k_y and ε, and associated with the Dirac points K and K'. The other parameters: $\lambda_0/M = 0.7$ and $M = 10$ meV. The red and blue lines correspond to the red and blue points marked on the dispersion curves in Fig. 2. The curves for the K and K' Dirac points are equivalent.

at the point x. This probability decays exponentially with the distance $|x|$ from the wall, though some oscillatory terms also appear due to imaginary components of the parameters κ. Following this, one can also find the corresponding expectation value of electron spin in the edge state described by the wave vector k_y,

$$\mathbf{s}_{k_y}(x) = \psi^{\dagger}_{k_y}(x)\,\boldsymbol{\sigma}\,\psi_{k_y}(x). \tag{15}$$

Components of the calculated spin density are presented in Fig. 4 as a function of x and for the energy and k_y corresponding to the red and blue points on the dispersion curves shown in Fig. 2. Only the nonzero components of spin density, i.e., the x and z ones, are shown there. The component of spin density along the Rashba wall, that is, the y component, vanishes exactly and it is not shown in Fig. 4. As one can note, the spin density decays exponentially with the distance $|x|$ from the wall, revealing, however, some oscillations that follow from the oscillations in the probability density with increasing distance from the wall. The calculated spin density depends not only on x, but also on k_y. This dependence is explicitly shown in the density plots of the x and z components of spin density, see Fig. 5. The top panels correspond to the upper energy branch (positive energy), whereas the lower one to the lower energy branch (negative energy). These figures clearly show the regions in the (k_y, x) space, where the particular spin components reach maximal and/or minimal values. For instance, the absolute value of the x component is maximal in the regime of small values of k_y, being positive (negative) for the upper (lower) energy branch. Behavior of the z component is qualitatively different and there are more areas of large z component. Note, the component along the domain wall, s_y, vanishes exactly for all values of k_y and all values of x, so it is not presented in Fig. 5.

The results on the spatial distribution of spin density associated with the edge electron states corresponding to wave vectors k_y, presented in Figs. 4 and 5, are the same for both

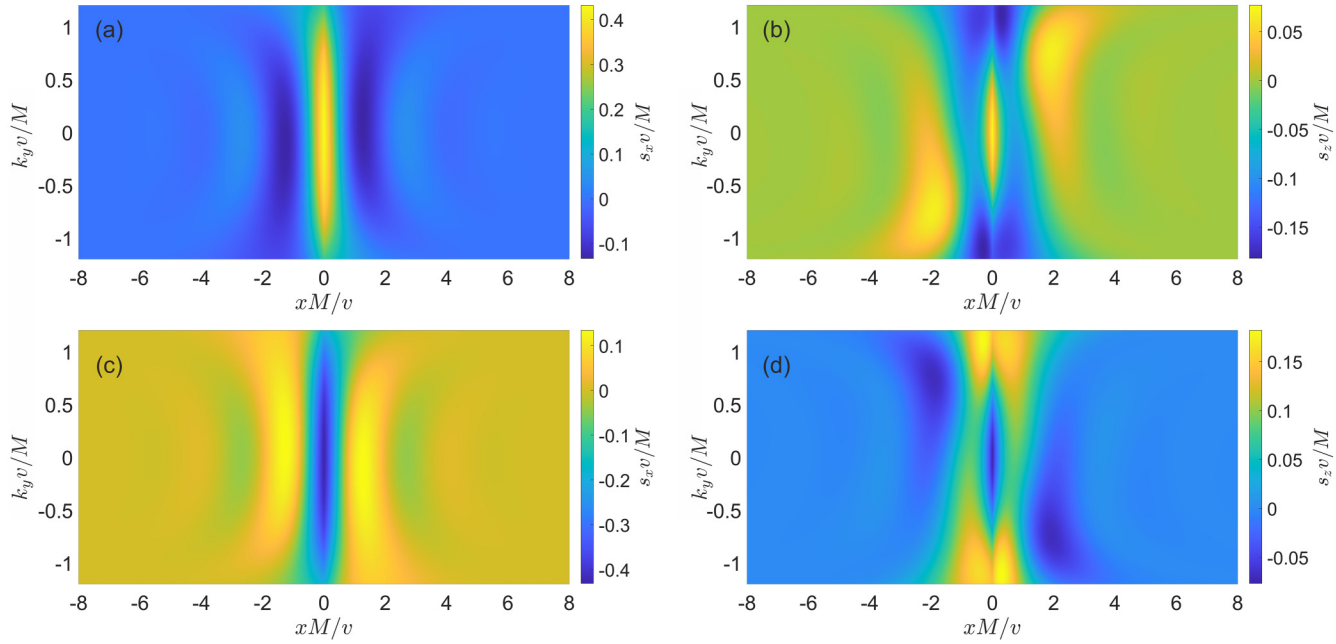

FIG. 5. The (a), (c) x and (b), (d) z components of spin density associated with the edge states localized at the Rashba domain wall, presented as a function of k_y and x. The top (bottom) panels correspond to the upper (lower) energy branch. The y component is not presented here as it vanishes for all values of k_y and x.

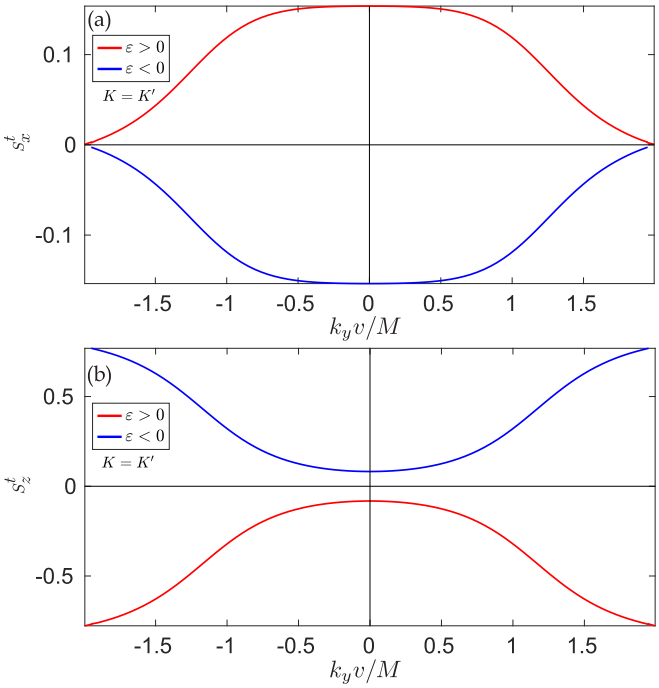

FIG. 6. The (a) x and (b) z components of the integrated spin in the edge states as a function of k_y. The red (blue) curves corresponds to the high (low) energy branch of the edge states. Here the energy of Rashba spin-orbit coupling is equal $\lambda_0 = M/2$.

Dirac valleys K and K'. These figures also show that the electron spin in an edge state for $\varepsilon > 0$ [upper energy band in Fig. 2(a)] is opposite to the electron spin in the corresponding state in the bottom energy band.

Figure 6 shows the integrated spin density $\mathbf{s}^t_{k_y}$ in the state k_y, calculated as

$$\mathbf{s}^t_{k_y} = \int_{-\infty}^{\infty} \mathbf{s}_{k_y}(x)\, dx. \tag{16}$$

The integrated spin density is shown there for the edge states of both higher ($\varepsilon > 0$) and lower ($\varepsilon < 0$) energy.

The absolute values of the x component of integrated spin are maximal for small wave vectors, whereas they decay to zero for the wave vectors, where the corresponding dispersion curves terminate (enter the relevant bulk bands). In turn, behavior of the z component of integrated spin is opposite, i.e., this component is small for small wave vectors and reaches the largest values at the points where the dispersion curves enter the bulk bands.

The total spin accumulated at the domain wall (per unit length of the wall) is presented in Fig. 7. Here we assumed that the Fermi level is located in the gap between the two branches of the edge states. Accordingly, the total spin includes the contributions of all edge states with energies $\varepsilon(k_y) < 0$,

$$\mathbf{S} = \sum_{K,K'} \int \frac{dk_y}{2\pi} \left(1 - \theta[\varepsilon(k_y)]\right) \mathbf{s}_{k_y}, \tag{17}$$

where $\theta(z)$ is the Heaviside's function. In addition, the contributions of both K and K' valleys are included. In this figure both x and z components of the spin accumulated at the

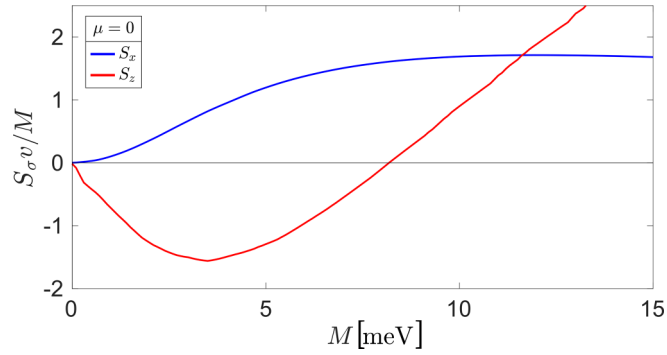

FIG. 7. The total spin per unit length accumulated at the domain wall as a function of magnetization M. Here the Fermi level is assumed in the gap, so the total spin includes contribution from the edge mode of lower energy.

wall are presented as a function of M. As expected, these two components vanish in the limit of $M \to 0$ as there are then no edge states (and no energy gap). The total spin components may in general change sign with increasing M.

III. INTERPLAY OF RASHBA AND MAGNETIC DOMAIN WALLS

A. General case and numerical results

From the above consideration we already know that topological properties of the edge states in case of individual Rasba wall in the presence of uniform magnetization are different from those of individual magnetic domain wall in a uniform Rashba field. As the edge states in the former case do not connect valence and conduction bands, and thus do not close the gap, they are not protected topologically. In turn, the edge states associated with magnetic domain wall connect the valence and conduction bands and thus close the energy gap and are related to the quantum anomalous Hall phase. It is interesting to explore the evolution of the edge states between these two limiting situations by varying the relevant parameters (magnetization and Rashba constant).

To do this we consider now a more general situation, when both Rashba and magnetic domain walls coexist, and we assume that the walls are located at the same positions, as shown schematically in Fig. 8. The interplay of both domain walls leads to interesting properties of the edge states. The results of numerical calculations are shown in Fig. 9, where

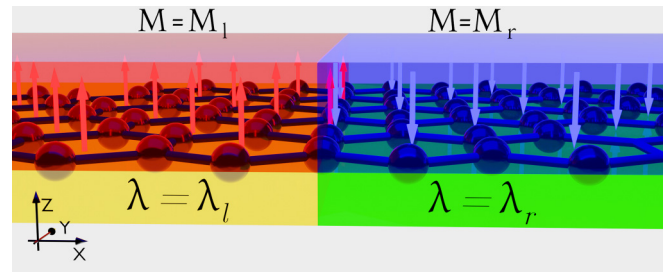

FIG. 8. Schematic picture of a graphene-based hybrid system with nonuniform Rashba spin-orbit coupling and nonuniform magnetization (coexisting Rashba spin-orbit and magnetic domain walls).

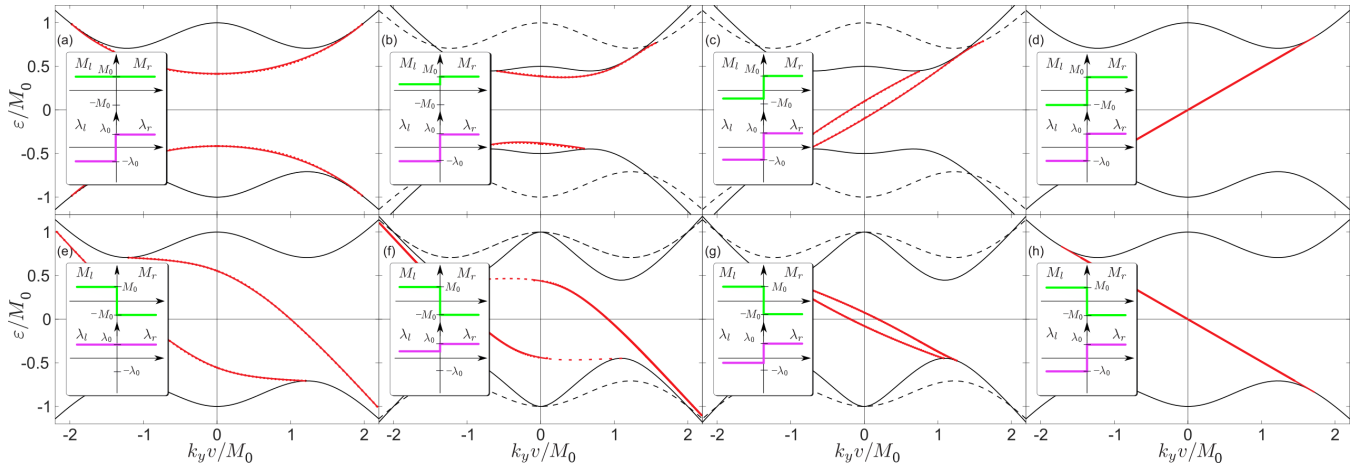

FIG. 9. Edge states for different parameters $[\lambda_l, \lambda_r]$ of Rashba coupling and different magnetizations $[M_l, M_r]$ on the left and right sides. Top panels: (a)–(d) $[\lambda_l, \lambda_r] = [-\lambda_0, \lambda_0]$, (a) $[M_l, M_r] = [M_0, M_0]$, (b) $[M_0/2, M_0]$, (c) $[-M_0/2, M_0]$, $[-M_0, M_0]$ (d). Bottom panels: (e)–(h) $[M_l, M_r] = [M_0, -M_0]$, (e) $[\lambda_l, \lambda_r] = [\lambda_0, \lambda_0]$, (f) $[\lambda_0/2, \lambda_0]$, (g) $[-\lambda_0/2, \lambda_0]$, (h) $[-\lambda_0, \lambda_0]$. Here, $\lambda_0 = 10$ meV and $M_0 = 10$ meV. The insets show schematically the corresponding magnitudes of $[M_l, M_r]$ and $[\lambda_l, \lambda_r]$, respectively).

we show the edge states in several situations, and for various combinations of the Rashba parameter and magnetization on both sides of the walls. Figures 9(a) and 9(e) correspond to individual Rashba and magnetic domain walls, respectively. The former situation was examined above, while the latter one was studied in our earlier work, see Ref. [2].

For clarity of terminology we note that when a certain parameter (magnetization or Rashba constant) has the same sign on both sides of the boundary, we refer to this situation as a step, while when this sign is opposite on both sides we call it domain wall (antisymmetric, when the corresponding absolute values of the parameter are the same on both sides, and asymmetric otherwise). In Figs. 9(a)–9(d) the antisymmetric Rashba domain wall (with opposite Rashba parameters on both sides of the wall) is fixed, while the magnetization changes from uniform [Fig. 9(a)] to the antisymmetric magnetic domain wall [Fig. 9(d)]. The situations in Figs. 9(b) and 9(c) correspond to magnetic step [Fig. 9(b)] and asymmetric domain wall [Fig. 9(c)], respectively. From Figs. 9(a)–9(d) it follows that when there is a magnetic domain wall in the presence of a Rashba domain wall, there are two edge states, which close the gap, independently if the magnetic wall is asymmetric or antisymmetric. However, in the absence of magnetic domain wall, the two edge states do not close the gap.

In turn, in Figs. 9(e)–9(h) the magnetic domain wall is fixed while the Rashba parameter changes from uniform [Fig. 9(e)] to the antisymmetric Rashba domain wall [Fig. 9(h)]. The situations in Figs. 9(f) and 9(g) correspond to different absolute values of the Rashba parameters on both sides of the magnetic wall; i.e., to a step [Fig. 9(f)] and asymmetric Rashba domain wall [Fig. 9(g)]. These figures allow us to generalize the conclusion from Figs. 9(a)–9(d) (see above) and state that when a magnetic domain wall exists, there are two edge states that connect valence and conduction bands closing the energy gap—independently of the Rashba parameters (except zero Rashba parameter, as there is then no gap and no edge states). Note, that magnetic domain walls (independently antisymmetric or asymmetric) exist in Figs. 9(c)–9(h), and in all these figures the edge states close the gap. This is because in all these situations the Chern numbers on both sides of the magnetiic domain wall are different, contrary to Figs. 9(a) and 9(b) where the Chern numbers on both sides are equal. However, chirality of the edge states in Figs. 9(c)–9(d) is opposite to that in Figs. 9(e)–9(h), which is due to the opposite signs of the magnetization in these two cases. Consequently, the Chern numbers have also opposite signs. According to the discussion in Ref. [2], there is an equilibrium current flowing along the wall, and the domain wall separates then two regions in the quantum anomalous Hall phase. Thus, when the Fermi level is located in the energy gap, one may expect the quantum anomalous Hall conductance of the system [45,46], $\sigma_{xy} = \frac{e^2}{h} n_{Ch}$, where

$$n_{\rm Ch} = \frac{1}{2\pi} \sum_{\nu} \sum_{n} \int d^2\mathbf{k}\, \Omega^{\nu}_{z,n}(\mathbf{k}) \equiv n^{K}_{\rm Ch} + n^{K'}_{\rm Ch} \qquad (18)$$

is the Chern number, and $\Omega^{\nu}_{z,n}(\mathbf{k})$ is the z component of the Berry curvature for the nth band in the momentum space (ν indicates two inequivalent Dirac points in graphene). For the effective continuum model describing bulk states in the system with a single magnetic domain, we find $n_{Ch} = 2\,\mathrm{sgn}(M)$, with the same contributions from the K and K' points, $n^{K}_{\rm Ch} = n^{K'}_{\rm Ch} = 1\,\mathrm{sgn}(M)$ [1,47–49]. From the bulk-boundary correspondence follows that two chiral edge modes can be expected at the interface between graphene and vacuum.

The system with a magnetic domain wall (independently of the presence or absence of Rashba kink or domain wall) can be treated as a junction of two QAH insulators with opposite chiralities of the localized edge states. As a result, there is a pair of topologically different topological insulators, $n_{\rm Ch}(x < 0) = 2$ and $n_{\rm Ch}(x > 0) = -2$, which correspond to the same symmetry class [50]. Thus, one may expect four localized states propagating along the domain wall in the same direction. The QAH conductivity at the domain wall is equal to $-4e^2/h$.

However, we note that the interface is not between topologically distinct insulators [50,51], so edge states are not protected against scattering. In other words, there are two topologically different phases, defined by different Chern numbers, but Hamiltonians describing these two regions belong to the same class of topological order. Secondly, the intervalley scattering processes are allowed for graphene, and these scattering processes are the main obstacle in realization of QAH effect in graphene-based systems.

In turn, the nonequilibrium charge and spin currents can be induced by external driving force, such as electric field or temperature gradient. This problem will be analyzed in the next section. It is also worth to note that the two edge states are degenerate in the case when both (Rashba and magnetic) domain walls are antisymmetric, see Figs. 9(d) and 9(h). In such a situation one can get simple analytical solutions for the energy of edge states. This peculiar situation will be analyzed in more detail in the following section.

B. Specific case of antisymmetric Rashba and magnetic domain walls

When the antisymmetric magnetic and Rashba domain walls coexist at the same position, energy of the edge states can be obtained in the analytical form. Taking into account Hamiltonian (1), modified by including magnetic domain wall, and following the method described above for the individual Rashba domain wall and in Ref. [2] for the individual magnetic wall, we arrive at the following formula for the energy of edge states localized at the antisymmetric double Rashba-magnetic domain wall in the form:

$$\varepsilon = \pm Q \frac{\hbar v_F}{2\lambda_0^2} k_y, \tag{19}$$

where v_F is the (Fermi) electron velocity in graphene, while

$$Q = \sqrt{2\left[M_0^2\left(M_0^2+4\lambda_0^2\right)\left(M_0^2+\lambda_0^2\right)^2\right]^{1/2} - 2M_0^4 - 6M_0^2\lambda_0^2} \tag{20}$$

and the $+$ and $-$ signs correspond to the configurations with $M_r > 0$ [Fig. 9(d)] and with $M_r < 0$ [Fig. 9(h)], respectively.

Properties of the above edge states differ qualitatively from those of the states localized at the individual Rashba domain wall studied above, as well as from properties of the individual magnetic domain studied in Ref. [2]. In the case of individual Rashba domain wall, the distribution of the probability density associated with a particular edge state is a symmetric function of x (the axis x is normal to the wall). The same is also true in the case of individual magnetic domain wall. In turn, in the case of antisymmetric double Rashba-magnetic domain wall, the probability density associated with a particular edge state is not symmetric. This is shown explicitly in Fig. 10 for both modes separately and for both Dirac points. The left panels corresponds to one the two edge state (solution for $A = B = 1$) and to the Dirac points K [Fig. 10(a)] and K' [Fig. 10(b)], while the right panels correspond to the second edge state (solution for $C = D = 1$) and to the Dirac points K [Fig. 10(d)] and K' [Fig. 10(e)]. In turn, Figs. 10(c) and 10(f) show the difference of the probabilities in the points K and K'. This difference is nonzero for both modes, and is shown explicitly in Fig. 10(c) for the first mode, and in Fig. 10(f) for the second mode. Accordingly, there is some asymmetry in the distribution of the probability density (i.e., charge density) between the two Dirac points. This property may be of some interest for valleytronics. We recall, that such a property is absent in the case of individual magnetic domain wall with uniform Rashba coupling and in case of Rashba domain with uniform magnetization. Obviously, the spin distribution corresponding to the considered here edge states associated with the antisymmetric magnetic-Rashba double domain wall is significantly different from the spin distribution for the edge states associated with an independent Rashba wall and uniform magnetization (see Fig. 5).

The spin density integrated over x and summed over the two edges states (i.e., the total spin associated with the edge state described by k_y), is shown in Fig. 11 for both K and K' Dirac points. This figure clearly shows the difference between spin values corresponding to k_y in the two Dirac points.

IV. NONEQUILIBRIUM TRANSPORT VIA CHIRAL STATES AT THE DOMAIN WALL

Now, let us consider nonequilibrium spin and charge transport via the chiral states at the composed (magnetic an Rashba) domain wall due to applied voltage or temperature gradient. To emphasize some basic features of these currents we assume the antisymmetric double domain wall, where the dispersion relation for both edge states is linear [these states are degenerate as already discussed above, see Figs. 9(d) and 9(h)]. This assumption allows to find simple analytical expressions for the currents.

A. Voltage-induced electric current

Let us consider one-dimensional electrons at the domain wall and assume the case of linear dispersion relation, Figs. 9(d) and 9(h). The corresponding spectrum is linear in k_y, $\varepsilon_k = \hbar v k_y$, where v the electron group velocity, $v = \pm(Q/2\lambda_0^2)v_F$, see Eqs. (19) and (20). In the following we limit ourselves to the case shown in Fig. 9(h). The corresponding v is then negative. Apart from this, it depends on M_0 and λ_0, and vanishes for $M_0 = 0$. We also assume that the electrons flowing along the wall are scattered only inelastically, e.g., from phonons, which leads to the energy relaxation. Using the kinetic equation for the distribution function in the stationary state and linear-response regime we find

$$eEv\frac{\partial f_0}{\partial \varepsilon} = -\frac{\delta f}{\tau_\varepsilon}, \tag{21}$$

where E is the external electric field along the wall, τ_ϵ is the energy relaxation time, $\delta f = f - f_0$, with $f_0(\varepsilon) = [e^{(\varepsilon-\mu)/k_BT}+1]^{-1}$ being the equilibrium distribution function and μ denoting the chemical potential. From Eq. (21) we get

$$\delta f = -eEv\tau_\varepsilon \frac{\partial f_0}{\partial \varepsilon}. \tag{22}$$

Importantly, we assumed here that the stationary state can be reached at the energy relaxation length $L_\varepsilon = |v|\tau_\varepsilon$, which should be smaller than the domain wall length, $L_\varepsilon \ll L$.

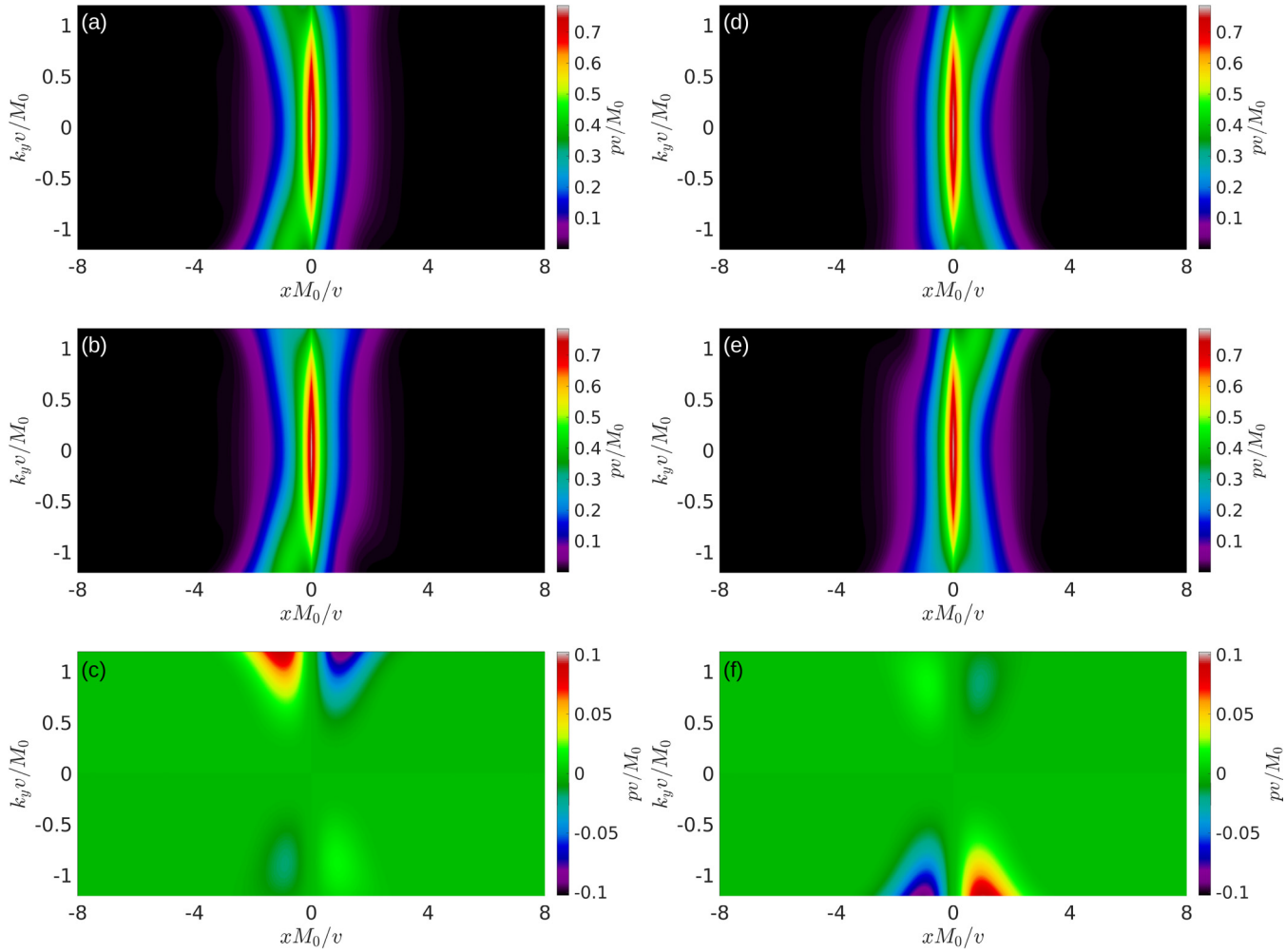

FIG. 10. Distribution of the probability density for electron states with linear spectrum and localized at the double domain wall (coexisting magnetic and Rashba antisymmetric domain walls). (a)–(c) present the probability density for one of the edge modes (corresponding to the solution $A, B = 1$), while (d)–(f) present the probability density for the second edge mode (corresponding to $C, D = 1$). (a), (d) correspond to Dirac point K while (b), (e) to K'. In turn (c), (f) show the difference of the probability density in the K and K' Dirac points for both edge modes.

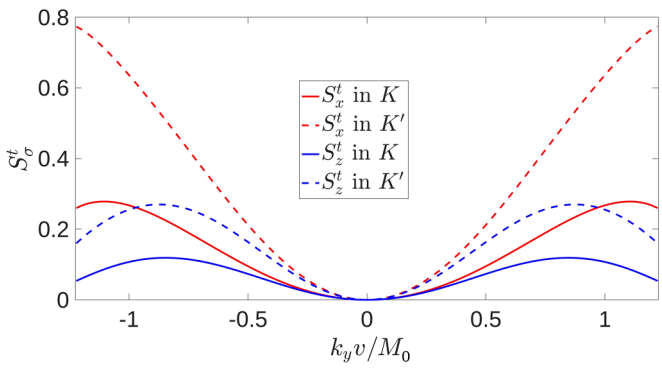

FIG. 11. The x and z components of the spin associated with the edge states, plotted as a function of k_y. Difference between the spins in the states corresponding to k_y and associated with the K and K' is clearly visible.

The nonequilibrium charge current due to electric field can be calculated as

$$I = 4ev \int \rho(\varepsilon)\,\delta f(\varepsilon)\,d\varepsilon = \frac{4e^2}{h} v\tau_\varepsilon E \int_{-\varepsilon_0}^{\varepsilon_0} \left(-\frac{\partial f_0}{\partial \varepsilon}\right) d\varepsilon, \tag{23}$$

where $h = 2\pi\hbar$, e^2/h is the conductance quantum (per quantum channel), $\rho(\varepsilon) = 1/2\pi\hbar|v|$ is the density of states (per channel), while $\varepsilon_0 \simeq \varepsilon_g/2$ determines the energy limits of the linear dispersion, with ε_g denoting the width of energy gap, within which the edge states propagate. The factor of 4 takes into account the two Dirac points and double degeneracy of the edge states in each Dirac point (i.e., there are four quantum transport channels). Note, the energy gap depends on M_0 and λ_0, and goes to zero when these parameters turn to zero.

We rewrite the above formula 23 in the form

$$I = \frac{4e^2}{h}\frac{L_\varepsilon}{L} V \int_{-\varepsilon_0}^{\varepsilon_0} \left(-\frac{\partial f_0}{\partial \varepsilon}\right) d\varepsilon, \tag{24}$$

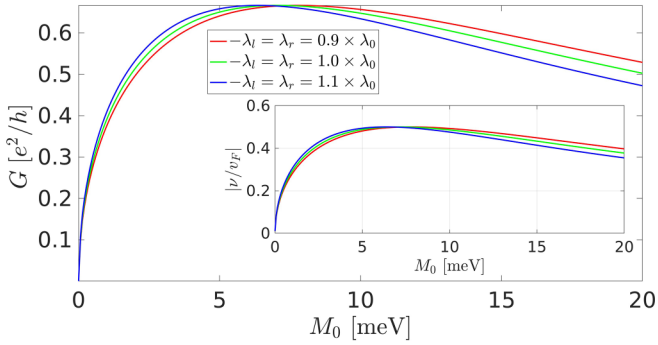

FIG. 12. Electrical conductance due to the edge states as a function of M_0, calculated for the DW length $L = 30\,\mu$m, $T = 0.1$ K, relaxation time $\tau_\varepsilon = 10$ ps, chemical potential $\mu = 10\,\mu$eV and $\lambda_0 = 10$ meV. The inset shows the absolute value of the corresponding electron velocity.

where V is voltage. Thus the conductance $G = I/V$ is

$$G = \frac{4e^2}{h}\frac{L_\varepsilon}{L}\int_{-\varepsilon_0}^{\varepsilon_0}\left(-\frac{\partial f_0}{\partial \varepsilon}\right)d\varepsilon. \tag{25}$$

At low temperatures, $k_BT \ll \varepsilon_0$, the integral in Eqs. (24) and (25) is equal to 1, and thus the conductance is $G = (4e^2/h)(L_\varepsilon/L)$.

Variation of conductance G with the parameters of the wall, i.e., with M_0 is shown in Fig. 12 for indicated values of λ_0. The conductance vanishes for $M_0 \to 0$, as in that limit there are no edge states. Then, the current increases with increasing M_0 and after reaching maximum at some value of M_0 it starts to decrease with a further increase in M_0. This behavior appears as a consequence of the variation of the electron velocity with increasing M_0, which (for a constant value of λ_0) first increases with increasing M_0 and then starts to decrease with M_0 after reaching the maximal value, see the inset in Fig. 12. A consequence of this decrease is a reduced conductance with increasing M_0 upon reaching the maximum value.

B. Spin Seebeck effect

A nonequilibrium current can also flow along the wall, when there is a nonzero temperature gradient along the wall. To find this current we assume that electron and phonon subsystems are in a local quasiequilibrium, $T_{el} = T_{ph} \equiv T$, so that the electron distribution function corresponds to quasiequilibrium at a local temperature of the lattice. This condition can be realized if $L_\varepsilon \ll L$.

Due to the linear dispersion relation and the particle-hole symmetry, the thermoelectric charge current vanishes as a result of the cancellations of particle and hole contributions to the charge current. This holds not only for the chemical potential $\mu = 0$ (middle of the gap) but also for μ shifted away (not to far) from the middle of the gap. However, the corresponding spin current vanishes only for $\mu = 0$, while for $\mu \neq 0$ it becomes nonzero. As one can see from Fig. 11, electronic states localized at the domain wall are spin polarized, and the expectation value of spin, $s_i(k_y) = \langle\sigma_i\rangle_{k_y}$, in the k_y state can be approximated by $s_i(k_y) = a_i k_y^2 + b_i k_y^4$. Here index $i = x, z$ corresponds to nonzero spin component (note that the y component of spin polarization is zero). The parameters a_i and b_i can be obtained by fitting to the data in Fig. 11. This figure shows total expectation values of spin components (including contributions from the two degenerate modes) in the K and K' Dirac points.

One can evaluate the thermoelectric spin current J_i^s along the domain wall as

$$\begin{aligned} J_i^s &= \nu\int\left[s_i^K(\varepsilon) + s_i^{K'}(\varepsilon)\right]\rho(\varepsilon)\,\delta f(\varepsilon)\,d\varepsilon \\ &= \frac{\tau_\varepsilon}{2\pi\hbar^3\nu}\frac{\nabla T}{T}\sum_{\chi=K,K'}\int_{-\varepsilon_0}^{\varepsilon_0}\left(a_i^\chi\varepsilon^2 + \frac{b_i^\chi\varepsilon^4}{\hbar^2\nu^2}\right)(\varepsilon-\mu) \\ &\quad\times\frac{\partial f_0}{\partial\varepsilon}\,d\varepsilon, \end{aligned} \tag{26}$$

where $\nabla T/T \ll 1$. At low temperatures, $k_BT < \varepsilon_0$, and for $\mu \neq 0$, the thermally generated spin current is

$$J_i^s \simeq -\frac{2\pi\tau_\varepsilon\mu k_B^2T^2}{3\hbar^3\nu}\frac{\nabla T}{T}\sum_{\chi=K,K'}\left(a_i^\chi + \frac{2b_i^\chi\mu^2}{\hbar^2\nu^2}\right), \tag{27}$$

where we used $\int_{-\infty}^{\infty}\frac{x^2dx}{\cosh^2 x} = \frac{\pi^2}{6}$. As the thermoelectric charge current vanishes in this limit, $I = 0$ (see the discussion above), we obtain a pure thermoelectric spin current.

V. SUMMARY AND CONCLUSIONS

We have derived analytical results for electronic states localized at the Rashba domain wall. Such a wall (antisymmetric or asymmetric) leads to edge states localized at the wall. These states emerge in the gap between conduction and valance bands and propagate along the wall. However, these states do not close the gap, i.e., they do not connect the conduction and valence bands. Thus, the gap survives, though it is remarkably reduced. Such a behavior is in agreement with equal topological Chern numbers on both sides of the Rashba domain wall.

We have also analyzed coexistence of the Rashba and magnetic domain walls in graphene, when both walls are sharp and located at the same position. In the absence of Rashba domain wall and for uniform Rashba field, the problem reduces to that analyzed in Ref. [2]. In a general case, independently of the presence or absence of the Rashba domain wall and independently if the magnetic wall is antisymmetric or asymmetric, the edge states emerge in the gap between conduction and valance bands and propagate along the wall. Moreover, these states connect the conduction and valence bands, and thus close the gap. This behavior is in agreement with different topological Chern numbers on both sides of the magnetic domain wall.

In the case of symmetric Rashba wall and uniform magnetization, dispersion relation of the edge states is symmetric

with respect to reversal of the propagation direction ($k_y \to -k_y$). In the vicinity of zero wave vector, the dispersion relation can be approximated by a parabolic band, and the corresponding effective electron mass can be then extremely large. This effective mass increases with increasing magnetization M and decreasing magnitude of the Rashba parameter λ_0. Such heavy fermions may be responsible for various specific transport properties of the states localized at the domain walls. In a general case, however, dispersion relations of the edge states are not symmetric in k_y.

The limit of antisymmetric Rashba and magnetic domain walls is particularly interesting as the dispersion curves of both edge states are then linear in k_y and degenerate. This holds for both K and K' Dirac points. Additionally, we have analyzed the spatial distribution of all components of the spin density associated with the edge states.

Apart from the equilibrium currents, we have also calculated the nonequilibrium charge and spin currents induced by electric field or temperature gradient. In the case of antisymmetric domain walls (with linear in k_y dispersion) we have derived some analytical results, and found that the thermally induced charge current vanishes, while the thermoelectric spin current is then nonzero.

ACKNOWLEDGMENTS

This work has been supported by the National Science Center in Poland under the project Sonata-14 No. 2018/31/D/ST3/02351.

APPENDIX: DERIVATION OF DISPERSION RELATION

To derive Eq. (10) we rewrite Eqs. (7) and (8) in the following form:

$$\psi_1(x,y) = e^{\kappa_1 x + ik_y y}\begin{pmatrix} 1 \\ \dfrac{-k_y^2v^2 + v^2\kappa_1^2 + M^2 - 2M\varepsilon + \varepsilon^2}{2v\lambda_0(k_y+\kappa_1)} \\ -i\dfrac{M-\varepsilon}{v(k_y+\kappa_1)} \\ i\dfrac{\left(-k_y^2v^2 + v^2\kappa_1^2 + M^2 - 2M\varepsilon + \varepsilon^2\right)(k_y-\kappa_1)}{2\lambda_0(k_y+\kappa_1)(\varepsilon+M)} \end{pmatrix} \equiv e^{\kappa_1 x + ik_y y}\begin{pmatrix} A_1 \\ B_1 \\ C_1 \\ D_1 \end{pmatrix} \tag{A1}$$

$$\psi_3(x,y) = e^{\kappa_3 x + ik_y y}\begin{pmatrix} 1 \\ \dfrac{-k_y^2v^2 + v^2\kappa_3^2 + M^2 - 2M\varepsilon + \varepsilon^2}{2v\lambda_0(k_y+\kappa_3)} \\ -i\dfrac{M-\varepsilon}{v(k_y+\kappa_3)} \\ i\dfrac{\left(-k_y^2v^2 + v^2\kappa_3^2 + M^2 - 2M\varepsilon + \varepsilon^2\right)(k_y-\kappa_3)}{2\lambda_0(k_y+\kappa_3)(\varepsilon+M)} \end{pmatrix} \equiv e^{\kappa_3 x + ik_y y}\begin{pmatrix} A_3 \\ B_3 \\ C_3 \\ D_3 \end{pmatrix} \tag{A2}$$

$$\psi_2(x,y) = e^{\kappa_2 x + ik_y y}\begin{pmatrix} 1 \\ -\dfrac{-k_y^2v^2 + v^2\kappa_2^2 + M^2 - 2M\varepsilon + \varepsilon^2}{2v\lambda_0(k_y+\kappa_2)} \\ -i\dfrac{M-\varepsilon}{v(k_y+\kappa_2)} \\ -i\dfrac{\left(-k_y^2v^2 + v^2\kappa_2^2 + M^2 - 2M\varepsilon + \varepsilon^2\right)(k_y-\kappa_2)}{2\lambda_0(k_y+\kappa_2)(\varepsilon+M)} \end{pmatrix} \equiv e^{\kappa_2 x + ik_y y}\begin{pmatrix} A_2 \\ B_2 \\ C_2 \\ D_2 \end{pmatrix} \tag{A3}$$

$$\psi_4(x,y) = e^{\kappa_4 x + ik_y y}\begin{pmatrix} 1 \\ -\dfrac{-k_y^2v^2 + v^2\kappa_4^2 + M^2 - 2M\varepsilon + \varepsilon^2}{2v\lambda_0(k_y+\kappa_4)} \\ -i\dfrac{M-\varepsilon}{v(k_y+\kappa_4)} \\ -i\dfrac{\left(-k_y^2v^2 + v^2\kappa_4^2 + M^2 - 2M\varepsilon + \varepsilon^2\right)(k_y-\kappa_4)}{2\lambda_0(k_y+\kappa_4)(\varepsilon+M)} \end{pmatrix} \equiv e^{\kappa_4 x + ik_y y}\begin{pmatrix} A_4 \\ B_4 \\ C_4 \\ D_4 \end{pmatrix} \tag{A4}$$

Since the real part of $\kappa_{1,3}$ is positive and of $\kappa_{2,4}$ negative we can write a general solution for the wave function corresponding to the localized state at the Rashba domain wall (this wave function exponentially decays with $x < 0$ and $x > 0$) as

$$\psi(x<0) = A\,\psi_1^<(x) + B\,\psi_3^<(x) \tag{A5}$$

$$\psi(x>0) = C\,\psi_2^>(x) + D\,\psi_4^>(x), \tag{A6}$$

where $\psi_{1,3}^<(x) \equiv \psi_{1,3}(x)$ and $\psi_{2,4}^>(x) \equiv \psi_{2,4}(x)$, and A, B, C, D are the coefficients, which can be determined from the continuity of the wave function at $x = 0$

$$A\,\psi_1^<(0) + B\,\psi_3^<(0) = C\,\psi_2^>(0) + D\,\psi_4^>(0). \tag{A7}$$

Substituting to (A5), (A6) corresponding expressions (A1)–(A4) for the wave functions $\psi_{1,3}^<(0)$ and $\psi_{2,4}^>(0)$ we come to four linear equations for the coefficients A, B, C, D

$$\begin{aligned} AA_1^< + BA_3^< - CA_2^> - DA_4^> &= 0,\\ AB_1^< + BB_3^< - CB_2^> - DB_4^> &= 0,\\ AC_1^< + BC_3^< - CC_2^> - DC_4^> &= 0,\\ AD_1^< + BD_3^< - CD_2^> - DD_4^> &= 0. \end{aligned} \tag{A8}$$

The determinant of this system of equations should be equal to zero, and this gives us the equation for energy

$$\det\begin{pmatrix} A_1^< & A_3^< & -A_2^> - A_4^> \\ B_1^< & B_3^< & -B_2^> - B_4^> \\ C_1^< & C_3^< & -C_2^> - C_4^> \\ D_1^< & D_3^< & -D_2^> - D_4^> \end{pmatrix} = 0. \tag{A9}$$

Using (A1)–(A4) and calculating determinant (A9) leads to Eq. (10) for the energy ε of the localized states

$$\frac{(-\varepsilon+M)\left[-\left\{\left(-2M^2-\lambda_0^2\right)\varepsilon^2 + M^2\lambda_0^2\right\}\xi(\zeta)\,\xi(-\zeta) + \lambda_0^2(-\varepsilon+M)(\varepsilon+M)\left(-v^2k_y^2 + M^2 + \varepsilon^2\right)\right]}{\lambda_0^2(\varepsilon+M)(M^2+\varepsilon^2-\zeta)(M^2+\varepsilon^2+\zeta)} = 0, \tag{A10}$$

which is exactly Eq. (10) in the main text, with $\xi(\zeta)$ and ζ defined below Eq. (10).

[1] A. Dyrdał and J. Barnaś, Anomalous, spin, and valley Hall effects in graphene deposited on ferromagnetic substrates, 2D Mater. **4**, 034003 (2017).

[2] M. Inglot, V. K. Dugaev, A. Dyrdał, and J. Barnaś, Graphene with Rashba spin-orbit interaction and coupling to a magnetic layer: Electron states localized at the domain wall, Phys. Rev. B **104**, 214408 (2021).

[3] M. S. Nevius, M. Conrad, F. Wang, A. Celis, M. N. Nair, A. Taleb-Ibrahimi, A. Tejeda, and E. H. Conrad, Semiconducting graphene from highly ordered substrate interactions, Phys. Rev. Lett. **115**, 136802 (2015).

[4] S. Sahu and G. C. Rout, Band gap opening in graphene: a short theoretical study, Int. Nano Lett. **7**, 81 (2017).

[5] J.-K. Lee, S. Yamazaki, H. Yun, J. Park, G. P. Kennedy, G.-T. Kim, O. Pietzsch, R. Wiesendanger, S. Lee, S. Hong, U. Dettlaff-Weglikowska, and S. Roth, Modification of electrical properties of graphene by substrate-induced nanomodulation, Nano Lett. **13**, 3494 (2013).

[6] C. Cardoso, D. Soriano, N. A. García-Martínez, and J. Fernández-Rossier, Van der Waals spin valves, Phys. Rev. Lett. **121**, 067701 (2018).

[7] Y. Han, L. Gao, J. Zhou, Y. Hou, Y. Jia, K. Cao, K. Duan, and Y. Lu, Deep elastic strain engineering of 2D materials and their twisted bilayers, ACS Appl. Mater. Interfaces **14**, 8655 (2022).

[8] E. Monazami, L. Bignardi, P. Rudolf, and P. Reinke, Strain lattice imprinting in graphene by C_{60} intercalation at the graphene/Cu interface, Nano Lett. **15**, 7421 (2015).

[9] A. Varykhalov, J. Sánchez-Barriga, A. M. Shikin, C. Biswas, E. Vescovo, A. Rybkin, D. Marchenko, and O. Rader, Electronic and magnetic properties of quasifreestanding graphene on Ni, Phys. Rev. Lett. **101**, 157601 (2008).

[10] F. Ellinger, C. Franchini, and V. Bellini, Magnetic 3*d* adatoms on free-standing and Ni(111)-supported graphene, Phys. Rev. Mater. **5**, 014406 (2021).

[11] N. Arabchigavkani, R. Somphonsane, H. Ramamoorthy, G. He, J. Nathawat, S. Yin, B. Barut, K. He, M. D. Randle, R. Dixit, K. Sakanashi, N. Aoki, K. Zhang, L. Wang, W.-N. Mei, P. A. Dowben, J. Fransson, and J. P. Bird, Remote mesoscopic signatures of induced magnetic texture in graphene, Phys. Rev. Lett. **126**, 086802 (2021).

[12] A. Kumar, S. Maiti, and D. L. Maslov, Zero-field spin resonance in graphene with proximity-induced spin-orbit coupling, Phys. Rev. B **104**, 155138 (2021).

[13] R. Sant, M. Cattelan, S. Agnoli, and G. Granozzi, Preparation and electronic structure of the WSe_2/graphene/$NiSe_x$/Ni(111) heterostructure, J. Vacuum Sci. Tech. A **39**, 052201 (2021).

[14] A. A. Gogina, A. G. Rybkin, A. M. Shikin, A. V. Tarasov, L. Petaccia, G. Di Santo, I. A. Eliseyev, S. P. Lebedev,

V. Y. Davydov, and I. I. Klimovskikh, Modification of the electronic structure of quasi-free-standing graphene by the adsorption and intercalation of Mn atoms, J. Exp. Theor. Phys. **132**, 906 (2021).

[15] S. Del Puppo, V. Carnevali, D. Perilli, F. Zarabara, A. L. Rizzini, G. Fornasier, E. Zupani, S. Fiori, L. L. Patera, M. Panighel, S. Bhardwaj, Z. Zou, G. Comelli, C. Africh, C. Cepek, C. Di Valentin, and M. Peressi, Tuning graphene doping by carbon monoxide intercalation at the Ni(111) interface, Carbon **176**, 253 (2021).

[16] M. N. Nair, A. Celis, F. Nicolas, S. Kubsky, A. Taleb-Ibrahimi, and A. Tejeda, Substrate effect on the electronic properties of graphene on vicinal Pt(111), Appl. Surf. Sci. **565**, 150593 (2021).

[17] M. Krivenkov, D. Marchenko, J. Sánchez-Barriga, E. Golias, O. Rader, and A. Varykhalov, Origin of the band gap in Bi-intercalated graphene on Ir(111), 2D Mater. **8**, 035007 (2021).

[18] S. S. P. Parkin, M. Hayashi, and L. Thomas, Magnetic domain-wall racetrack memory, Science **320**, 190 (2008).

[19] Q. Li, C. X. Trang, W. Wu, J. Hwang, D. Cortie, N. Medhekar, S.-K. Mo, S. A. Yang, and M. T. Edmonds, Large magnetic gap in a designer ferromagnet-topological insulator-ferromagnet heterostructure, Adv. Mater. **34**, 2107520 (2022).

[20] M. Sedlmayr, N. Sedlmayr, J. Barnaś, and V. K. Dugaev, Chiral Hall effect in the kink states in topological insulators with magnetic domain walls, Phys. Rev. B **101**, 155420 (2020).

[21] L. Fu and C. L. Kane, Superconducting proximity effect and Majorana fermions at the surface of a topological insulator, Phys. Rev. Lett. **100**, 096407 (2008).

[22] I. M. Khaymovich, N. B. Kopnin, A. S. Mel'nikov, and I. A. Shereshevskii, Vortex core states in superconducting graphene, Phys. Rev. B **79**, 224506 (2009).

[23] X. Chen and V. I. Fal'ko, Hierarchy of gaps and magnetic minibands in graphene in the presence of the Abrikosov vortex lattice, Phys. Rev. B **93**, 035427 (2016).

[24] I. Martin, Y. M. Blanter, and A. F. Morpurgo, Topological confinement in bilayer graphene, Phys. Rev. Lett. **100**, 036804 (2008).

[25] F. Zhang, A. H. MacDonald, and E. J. Mele, Valley Chern numbers and boundary modes in gapped bilayer graphene, Proc. Natl. Acad. Sci. USA **110**, 10546 (2013).

[26] A. Vaezi, Y. Liang, D. H. Ngai, L. Yang, and E.-A. Kim, Topological edge states at a tilt boundary in gated multilayer graphene, Phys. Rev. X **3**, 021018 (2013).

[27] N. S. Baßler and K. P. Schmidt, Effects of domain walls in bilayer graphene in an external magnetic field, Phys. Rev. B **103**, 155422 (2021).

[28] P. Anderson, Y. Huang, Y. Fan, S. Qubbaj, S. Coh, Q. Zhou, and C. Ojeda-Aristizabal, Strain-tuning of domain walls in multilayer graphene probed in the quantum Hall regime, Phys. Rev. B **105**, L081408 (2022).

[29] J.-B. Touchais, P. Simon, and A. Mesaros, Robust propagating in-gap modes due to spin-orbit domain walls in graphene, Phys. Rev. B **106**, 035139 (2022).

[30] M. Rataj and J. Barnaś, Graphene p-n junctions with nonuniform Rashba spin-orbit coupling, Appl. Phys. Lett. **99**, 162107 (2011).

[31] M. Rataj and J. Barnaś, Transmission through graphene junctions with Rashba spin-orbit coupling, Acta Phys. Pol. A **127**, 481 (2015).

[32] M. Rataj and J. Barnaś, Large anisotropic magnetoresistance in graphene-based junctions, Phys. Status Solidi RRL **7**, 997 (2013).

[33] T. Hu, F. Jia, G. Zhao, J. Wu, A. Stroppa, and W. Ren, Intrinsic and anisotropic Rashba spin splitting in Janus transition-metal dichalcogenide monolayers, Phys. Rev. B **97**, 235404 (2018).

[34] D. Leykam, A. Andreanov, and S. Flach, Artificial flat band systems: from lattice models to experiments, Adv. Phys.: X **3**, 1473052 (2018).

[35] R. Bistritzer and A. H. MacDonald, Moiré bands in twisted double-layer graphene, Proc. Natl. Acad. Sci. USA **108**, 12233 (2011).

[36] E. K. Petrov, V. N. Men'shov, I. P. Rusinov, M. Hoffmann, A. Ernst, M. M. Otrokov, V. K. Dugaev, T. V. Menshchikova, and E. V. Chulkov, Domain wall induced spin-polarized flat bands in antiferromagnetic topological insulators, Phys. Rev. B **103**, 235142 (2021).

[37] A. L. Sharpe, E. J. Fox, A. W. Barnard, J. Finney, K. Watanabe, T. Taniguchi, M. A. Kastner, and D. Goldhaber-Gordon, Emergent ferromagnetism near three-quarters filling in twisted bilayer graphene, Science **365**, 605 (2019).

[38] E. S. Morell, J. D. Correa, P. Vargas, M. Pacheco, and Z. Barticevic, Flat bands in slightly twisted bilayer graphene: Tight-binding calculations, Phys. Rev. B **82**, 121407(R) (2010).

[39] M. Yankowitz, S. Chen, H. Polshyn, Y. Zhang, K. Watanabe, T. Taniguchi, D. Graf, A. F. Young, and C. R. Dean, Tuning superconductivity in twisted bilayer graphene, Science **363**, 1059 (2019).

[40] H. C. Po, L. Zou, A. Vishwanath, and T. Senthil, Origin of Mott insulating behavior and superconductivity in twisted bilayer graphene, Phys. Rev. X **8**, 031089 (2018).

[41] B. Lian, Z. Wang, and B. A. Bernevig, Twisted bilayer graphene: A phonon-driven superconductor, Phys. Rev. Lett. **122**, 257002 (2019).

[42] C.-C. Liu, L.-D. Zhang, W.-Q. Chen, and F. Yang, Chiral spin density wave and $d + id$ superconductivity in the magic-angle-twisted bilayer graphene, Phys. Rev. Lett. **121**, 217001 (2018).

[43] C. L. Kane and E. J. Mele, Quantum spin Hall effect in graphene, Phys. Rev. Lett. **95**, 226801 (2005).

[44] E. I. Rashba, Graphene with structure-induced spin-orbit coupling: Spin-polarized states, spin zero modes, and quantum Hall effect, Phys. Rev. B **79**, 161409(R) (2009).

[45] D. J. Thouless, M. Kohmoto, M. P. Nightingale, and M. den Nijs, Quantized Hall conductance in a two-dimensional periodic potential, Phys. Rev. Lett. **49**, 405 (1982).

[46] Q. Niu, D. J. Thouless, and Y.-S. Wu, Quantized Hall conductance as a topological invariant, Phys. Rev. B **31**, 3372 (1985).

[47] Z. Qiao, S. A. Yang, W. Feng, W.-K. Tse, J. Ding, Y. Yao, J. Wang, and Q. Niu, Quantum anomalous Hall effect in graphene from Rashba and exchange effects, Phys. Rev. B **82**, 161414(R) (2010).

[48] Z. Qiao, H. Jiang, X. Li, Y. Yao, and Q. Niu, Microscopic theory of quantum anomalous Hall effect in graphene, Phys. Rev. B **85**, 115439 (2012).

[49] P. Högl, T. Frank, K. Zollner, D. Kochan, M. Gmitra, and J. Fabian, Quantum anomalous Hall effects in graphene from proximity-induced uniform and staggered spin-orbit and exchange coupling, Phys. Rev. Lett. **124**, 136403 (2020).

[50] C.-K. Chiu, J. C. Y. Teo, A. P. Schnyder, and S. Ryu, Classification of topological quantum matter with symmetries, Rev. Mod. Phys. **88**, 035005 (2016).

[51] J. Cayssol, Introduction to Dirac materials and topological insulators, C. R. Phys. **14**, 760 (2013).